LRO/LAMP observations of the lunar helium exosphere: constraints on thermal accommodation and outgassing rate

Cesare Grava [1]★ Dana M. Hurley [2] Paul D. Feldman [3] Kurt D. Retherford [1]
Thomas K. Greathouse [1] Wayne R. Pryor [4] G. Randall Gladstone [1] Jasper S. Halekas [5]
Kathleen E. Mandt [2] Danielle Y. Wyrick,[1] Michael W. Davis [1] Anthony F. Egan,[6]
David E. Kaufmann,[6] Maarten H. Versteeg [1] and S. Alan Stern [6]

[1] *Southwest Research Institute, 6220 Culebra road, San Antonio, TX 78238, USA*
[2] *Johns Hopkins University, Applied Physics Laboratory, Laurel, MD 20723, USA*
[3] *Department of Physics and Astronomy, Johns Hopkins University, Baltimore, MD 21218, USA*
[4] *Central Arizona College, Coolidge, AZ 85128, USA*
[5] *Department of Physics and Astronomy, University of Iowa, Iowa City, IA 52242, USA*
[6] *Southwest Research Institute, Boulder, CO 80302, USA*

ABSTRACT

We report a comprehensive study by the UV spectrograph LAMP (Lyman-Alpha Mapping Project) onboard the Lunar Reconnaissance Orbiter to map the spatial distribution and temporal evolution of helium atoms in the lunar exosphere, via spectroscopy of the He I emission line at 58.4 nm. Comparisons with several Monte Carlo models show that lunar exospheric helium is fully thermalized with the surface (accommodation coefficient of 1.0). LAMP-derived helium source rates are compared to the flux of solar wind alpha particles measured *in situ* by the *ARTEMIS* twin spacecraft. Our observations confirm that these alpha particles (He^{++}) are the main source of lunar exospheric helium, representing 79 per cent of the total source rate, with the remaining 21 per cent presumed to be outgassing from the lunar interior. The endogenic source rate we derive, $(1.49 \pm 0.08) \times 10^6$ cm^{-2} s^{-1}, is consistent with previous measurements but is now better constrained. LAMP-constrained exospheric surface densities present a dawn/dusk ratio of ∼1.8, within the value measured by the Apollo 17 surface mass spectrometer LACE (Lunar Atmosphere Composition Experiment). Finally, observations of lunar helium during three Earth's magnetotail crossings, when the Moon is shielded from the solar wind, confirm previous observations of an exponential decay of helium with a time constant of 4.5 d

Key words: techniques: spectroscopic – solar wind – Sun: UV radiation – Moon.

1 INTRODUCTION

Helium was among the first elements discovered in the lunar exosphere, by the Lunar Atmosphere Composition Experiment (LACE) mass spectrometer deployed on the lunar surface by the astronauts of the Apollo 17 mission (Hoffman et al. 1973). Together with argon-40 (^{40}Ar), helium is the most abundant element in the lunar exosphere detected so far, peaking at a few 10^4 cm^{-3} shortly after mid-night local time (LT). It was detected spectroscopically for the first time by Stern et al. (2012) using the Lyman-Alpha Mapping Project (LAMP; Gladstone et al. 2010) aboard the *Lunar Reconnaissance Orbiter* (*LRO*; Chin et al. 2007) thanks to its relatively bright resonant fluorescence emission line at 58.4 nm.

1.1 Relationship with the solar wind

The main source for the lunar exospheric helium is the solar wind, as demonstrated by the correlation between exospheric helium density

and the geomagnetic index Kp, a proxy for solar wind density (Wilcox, Schatten & Ness 1967; Hodges & Hoffman 1974). The source mechanism for helium is neutralization of solar wind alpha particles (^{4}He^{++}) upon impact on the lunar surface. As the Moon enters the Earth's magnetosphere, which stands off the solar wind, the exospheric helium density begins to decrease: previous LAMP observations (Feldman et al. 2012) recorded a factor of 2 decrease within the 5-d passage of the Moon through Earth's magnetotail ($\pm 25°$ from full Moon). Subsequently, repeated *in situ* detections of helium by the Neutral Mass Spectrometer (NMS) aboard the *Lunar Atmosphere and Dust Environment Explorer* (*LADEE*) confirmed the 4.5-d escape time constant (Benna et al. 2015), and confirmed that gravitational escape is the dominant loss process for lunar helium, with photoionization being a secondary but non-negligible loss process (Hodges, Hoffman & Johnson 1974).

1.2 Lunar outgassing of radiogenic elements

Searches for lunar outgassing began with data from the Apollo instruments, first with the surface-based Suprathermal Ion Detector

★ E-mail: cgrava@swri.edu

Experiment (Benson, Freeman & Hills 1975; Freeman & Benson 1977) then with the Apollo 15 and 16 orbital mass spectrometers (Hodges 1972; Hodges et al. 1972, 1973). The most compelling evidence for it arose from measurements of argon: peaks in exospheric densities of ^{40}Ar measured by LACE were correlated with moonquakes registered by the Apollo seismometers (Hodges 1977b; Nakamura et al. 1979). Argon-40 is a product of the radiogenic decay of ^{40}K within the crust, which outgases into the exosphere after shallow moonquakes that open cracks or fissures in the upper crust (Killen 2002). In this case, other radiogenic elements can outgas as well, such as helium. Even if the vast majority of lunar exospheric helium ultimately comes from the solar wind, it was acknowledged soon after its discovery that a small fraction of it originates from the interior of the Moon. In fact, helium is the daughter of the radioactive decay of ^{232}Th, ^{238}U, and ^{235}U within the crust (Kockarts 1973). Cook & Stern (2014) reported 'helium flares', or enhancements in exospheric lunar helium density measured by LAMP with no apparent correlation with solar wind alpha particles flux or with meteoroid activity (which affect the release of other, condensable species, such as Na, K, and H_2O). As discussed by Cook & Stern (2014), these 'helium flares' revamped Hodges (1977b) hypothesis that at least some fraction of the lunar exospheric helium comes from the interior of the Moon. Finally, *LADEE*'s NMS *in situ* measurements implied that the source rate from degassing of endogenic helium is 15 per cent of the solar wind alpha particles source rate (Benna et al. 2015), while *LRO*'s LAMP brightness (remote sensing) allowed for a greater fraction: 30–40 per cent (Grava et al. 2016; Hurley et al. 2016).

1.3 Helium interaction with the lunar surface

Once the solar wind alpha particles are released from the grains as neutral helium, atoms bounce in ballistic trajectories across the lunar surface, until they are lost from the system (via thermal escape or photoionization). Perhaps the most controversial aspect of the lunar helium (or of any other gas in the lunar exosphere) is the gas–surface interaction, i.e. what happens when a helium atom encounters the lunar surface. The debate whether or not the helium atoms were thermally accommodated to the lunar surface is evident in the series of papers by Hodges (1973) and Hartle, Curtis & Thomas (1975) on one side, favouring full thermal accommodation, and Shemansky & Broadfoot (1977) and Smith et al. (1978) on the other side, arguing against it. Thermal accommodation can be described by the accommodation coefficient α (Hunten, Morgan & Shemansky 1988):

$$\alpha = \frac{E_{\text{out}} - E_{\text{in}}}{E_{\text{T}} - E_{\text{in}}}, \tag{1}$$

where E_{in} is the energy of the impacting helium atom, E_{out} is the energy of the atom leaving the surface, and E_{T} is the energy of the atom in thermal equilibrium with the surface. Equation (1) can be rewritten as $E_{\text{out}} = E_{\text{in}} + \alpha \times (E_{\text{T}} - E_{\text{in}})$. An accommodation coefficient of 1.0 implies $E_{\text{out}} = E_{\text{T}}$, meaning that the atom leaves the surface with an energy corresponding to the thermal equilibrium with the surface, without any memory of its energy prior to the collision. This full thermal accommodation was generally accepted by several modelers in the early attempts to reproduce the lunar helium exosphere observations by LACE (Hartle & Thomas 1974; Hodges 1975). The assumption was justified by the saturation of the lunar surface with helium, which, on the basis of the solar wind flux measured at the lunar surface by the Apollo 11 Solar Wind Composition Experiment (Buhler et al. 1969), should occur

within 10^3–10^4 yr (Banks, Johnson & Axford 1970; Kumar 1976). Therefore, for every solar wind alpha particle that implants itself on to the lunar surface, a helium atom is released into the exosphere with energy that depends on the surface temperature. This assumption of saturation was challenged later by Shemansky & Broadfoot (1977) and Smith et al. (1978). The impetus was the mismatch between exospheric models and far-ultraviolet (FUV) spectra taken from the Mariner 10 Ultraviolet Spectrometer of Mercury's exosphere, considered to be very similar to the Moon's in terms of dynamics. The mismatch was particularly evident for observations taken close to the terminators and on the nightside (Broadfoot, Shemansky & Kumar 1976). Conversely, the match between observations and models was good for dayside regions, where the temperature is well known and uniform. Shemansky & Broadfoot (1977) and Smith et al. (1978) noted that the interaction between the helium atoms and the surface involves single phonon collisions rather than multiple ones, and that α depends on the Debye characteristic temperature of the crystal. The time τ available to a single helium atom to interact with a grain of the surface is

$$\tau = \tau_0 \exp\left(\frac{Q}{RT}\right), \tag{2}$$

where τ_0 is a statistical vibration period, R the gas constant, Q the heat of adsorption, and T the temperature (Hunten et al. 1988). The $\exp(Q/RT)$ factor represents the number of collisions between the atom and the surface. For helium colliding with a 200 K surface, $\tau \sim \tau_0 = 10^{-12}$ s, too small to allow exchange of energy between the gas and the surface. But Hodges (1980a) noted that the porosity of the lunar soil grains might increase this adsorption time. The upper regolith (or epiregolith) is a fairy-castle structure of loosely packed grains. Hence, upon neutralization of a solar wind alpha particle, the freshly created helium atom has a high probability of colliding with another grain. Hodges (1980a) calculations suggest that each helium atom on average experiences ∼6 collisions with surface grains before diffusing out into the exosphere. This should allow enough time for the particles to thermalize with the surface.

This debate (see also Shemansky 1980; Hodges 1980b) has implications that go beyond academic discussions. Thermal accommodation controls the escape rate and thus the exospheric density, as we shall see in Section 3. More recently, Leblanc & Chaufray (2011) applied a Monte Carlo simulation of the lunar exosphere to re-analyse and compare published Mariner 10 spectra of Mercury and LACE exospheric densities of the Moon. Although they found that an accommodation coefficient larger than 0.75 is consistent with LACE data, a model with a nightside accommodation coefficient lower than that on the dayside might also be consistent with the data. The debate regarding the accommodation coefficient of the airless bodies Mercury and Moon did not progress much further because of lack of observations.

1.4 Objectives of this study

In this paper, we describe observations of the lunar exospheric helium aimed to address these outstanding questions, and their comparison with our best exospheric model. The goal of these observations is to study the dependence of lunar helium density on LT, solar wind conditions, and longitude. Each of these three dependencies is informative about a specific aspect of the lunar helium. For example, the dependence of helium density on LT, and hence on lunar surface temperature, constrains the degree of accommodation between helium atoms and the surface. And the dependence of helium density on the solar wind alpha flux constrains the endogenic source

rate and the response of the exosphere to the solar wind variations. Observations to address these objectives were performed by LAMP, the UV imaging spectrograph aboard the *LRO*.

2 OBSERVATIONS AND DATA REDUCTION

LRO is a polar orbiter. At least twice per orbit, in its nominal nadir pointing, LAMP will observe the lunar night side while the spacecraft is illuminated. In this case, the column of gas between the spacecraft and the shadow point (the point where LAMP line of sight encounters the Moon's shadow) will resonantly scatter solar UV photons. To measure the lunar helium density, we take advantage of this resonant scattering in the Extreme Ultraviolet (EUV), at 58.4 nm. These 'twilight' observations occur in pairs (one at each pole) for just a few minutes within each orbit. Several of these twilight observations must be co-added to produce a spectrum with reliable signal-to-noise ratio (SNR). These observations are useful for exospheric composition studies (e.g. Cook et al. 2013), but do not allow one to follow trends in time or latitude. Better SNR during nadir-pointing observations is achieved when *LRO*'s so-called beta-angle (the angle between the spacecraft orbital plane and the Sun–Moon direction) is near 90°, and the spacecraft is thus orbiting close to the terminator plane. In this case, it is possible to observe the lunar exosphere for almost the entirety of the nightside half-orbit, but this configuration occurs only twice per year and for a few days each time and only at very limited LTs (dawn and dusk). In this paper, we analyse observations taken during ad hoc off-nadir geometries called roll and pitch slews. Roll slews occur when the spacecraft is tilted laterally with respect to the direction of motion. Pitch slews are tilts (both backward and forward) along the direction of motion.

The LAMP field of view must not contain any portion of the lunar dayside. Although the solar spectrum is orders of magnitude dimmer in the EUV compared to the FUV, dayside observations are only feasible with the instrument's door closed, when the light passes through a pinhole whose area is ∼740 times smaller than the full aperture. This is needed since the LAMP bandpass (∼57–195 nm) includes the FUV, where sunlight reflected off the dayside surface is much brighter than in the EUV; without this measure, the detector would be swamped in counts from the longer wavelength lunar reflection. Roll slews are the easiest to interpret, because the LT of the shadow point is close to the LT of the spacecraft, hence the density of the exospheric helium does not vary dramatically along the line of sight. Pitch slews are more difficult to interpret because the LT can vary substantially from the spacecraft to the shadow point. See Fig. 1 for an example. In this figure, the LT of *LRO* changes considerably, from ∼21:00 LT for the first observation (violet sector) to ∼08:00 LT for the last one (orange sector), while the LT of the shadow point is always near ∼21:00 LT. The exospheric helium density varies with the LT. For example, at the surface level it peaks at approximately ∼02:00 LT (a consequence of the combination of lower nighttime surface temperature, and hence shorter hops between encounters with the surface, and the migration from the hot dayside of helium atoms) and minimum at noon (see e.g. Fig. 9). Therefore, to compare model with data one has to compute the LT at every step along the line of sight. This procedure is described in detail in Section 3.1. Also note that in this particular case (Fig. 1), the shadow point at the beginning of the scan (violet sector) was quite high, at ∼150 km above the lunar surface. Roll slews were analysed in Grava et al. (2016) but are also reported here for completeness.

Table 1 lists a sample of all the LAMP data used, the start and end times of the observations, and the type of maneuver (negative angles
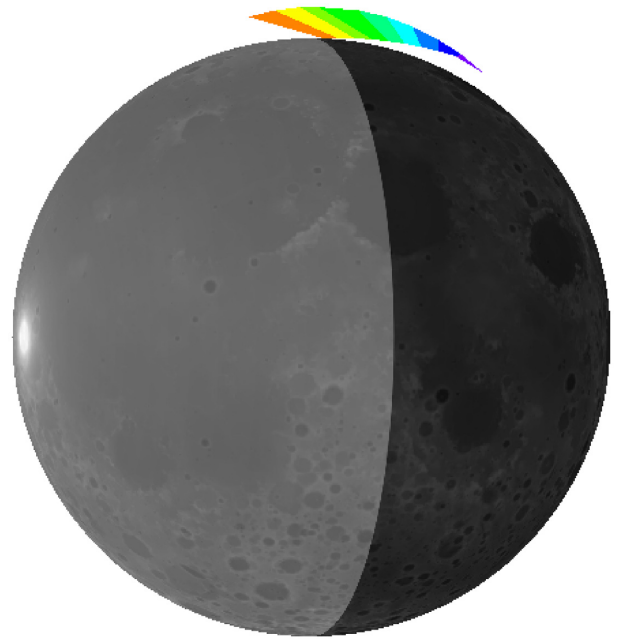

Figure 1. Representation of a pointing geometry. The Moon (represented here with a topographic map from *LRO*'s LOLA altimeter) is viewed as from the Northern hemisphere. Each coloured section represents one 2-min bin of LAMP illuminated field of view where helium signal is collected. The colours indicate temporal evolution of the orbit, with warmer colours occurring later in time. Whiter shading of the Moon represents with fidelity the solar illumination for this particular date (2013 October 25), with the subsolar point around the Western maria. The figure is to scale, with *LRO*'s orbit represented by the top of the coloured sections. The bottom of the coloured sections represents the shadow point.

mean pitch backwards with respect to the direction of motion). The full table is available in the online version of the paper.

2.1 Extraction of brightness and background subtraction

LAMP is an imaging spectrograph with the capability of recording the time, wavelength, and the detector row, i.e. the location, along the slit's length (6°), of each detected photon. *LRO* completes a lunar orbit in about 2 h, roughly half of which is over the nightside (depending on the beta angle). For each orbit, we restricted our analysis to the timeframe when the spacecraft was illuminated and the instrument was pointing to the lunar nightside (from a minimum of 4 min to a maximum of 38 min), then subdivided this timeframe to 2-min intervals, roughly the time it takes for the LAMP field of view to cover 10° in latitude. For each of these bins, we extracted LAMP's measured 58.4 nm brightness in count s^{-1} by collecting the light from all the illuminated rows of the detector. (i.e. from the 5th to the 25th inclusive) and from columns 131 and 149 of the detector, corresponding to a wavelength range of 57.6–60.9 nm. Since irradiance from stars is negligible in the EUV wavelength region, the dominant source of background at this wavelength (58.4 nm) is the lunar surface reflection of the resonantly scattered solar photons by the interstellar helium passing through the heliosphere. This interplanetary helium emission is faint (a few Rayleighs at most) but LAMP can detect such a small brightness. For each maneuver, the background consisted of the average over several LAMP spectra of the lunar surface taken with the spacecraft in shadow and with an off-nadir angle (either roll or pitch) within 3° from the 'nominal' off-

Table 1. Sample list of LAMP data used. The complete table can be found in the online version of the article.

File name	Start mid-time (UT)	End mid-time (UT)	Type of maneuver	g-factor (s^{-1})	Solar wind flux (cm^{-2} s^{-1})
LAMP_ENG_0403182883_02.fit	2013-10-11T12:34:08.00	2013-10-11T12:46:08.00	pitch $-63°$	1.17E−005	9.73E+008
LAMP_ENG_0406951440_02.fit	2013-11-24T02:37:12.00	2013-11-24T02:41:12.00	pitch 75°	1.07E−005	5.15E+008
LAMP_ENG_0408732396_02.fit	2013-12-14T17:29:43.00	2013-12-14T17:43:43.00	roll 25°	1.30E−005	9.92E+008
LAMP_ENG_0409308372_02.fit	2013-12-21T09:08:06.00	2013-12-21T09:18:06.00	roll $-60°$	1.14E−005	4.10E+008
LAMP_ENG_0410325183_02.fit	2014-01-02T03:41:12.00	2014-01-02T03:47:12.00	pitch 63°	1.19E−005	8.02E+008
LAMP_ENG_0412031647_02.fit	2014-01-21T21:41:56.00	2014-01-21T21:49:56.00	pitch 64°	1.16E−005	8.00E+008
LAMP_ENG_0453197832_02.fit	2015-05-13T09:05:55.00	2015-05-13T09:39:55.00	pitch 31°	1.14E−005	1.49E+009
LAMP_ENG_0454508668_02.fit	2015-05-28T12:56:40.00	2015-05-28T13:08:40.00	pitch 43°	8.30E−006	1.02E+009

nadir angle of that maneuver (e.g. 40°–46° for pitches 43°). In this way, we are averaging spectra taken over disparate lunar locations, therefore smoothing differences in albedo for the background signal. Fig. 2 illustrates the extraction of the signal from one spectrum.

After the subtraction of the background, we compute the sum over the emission line (region encompassed by the vertical lines in Fig. 2) and we convert it from counts s^{-1} to Rayleighs (1 R = $10^6/4\pi$ photons cm^{-2} s^{-1} sr^{-1}; Hunten, Roach & Chamberlain 1956) using the calibration factor of 0.485 counts s^{-1} Rayleigh^{-1} derived from LAMP observations of interstellar helium (Grava et al. 2018). Finally, the brightness in Rayleighs is converted into column density using solar irradiance at 58.4 nm. The He I fluorescence emission line is in fact due to a return to the ground state of a helium atom's electron previously excited by a solar photon. For optically thin exospheres, there is a linear relationship between column density and measured brightness, and these are related by the so-called g-factor (number of solar photons resonantly scattered by each helium atom each second):

$$B = \frac{gN}{10^6},\tag{3}$$

where B is the brightness expressed in Rayleighs (R), N is the column density expressed in atoms cm^{-2}, and the g-factor g is in photons atom^{-1} s^{-1}, and is directly related to the solar irradiance (Barth 1969). For solar irradiance, we relied upon data from the Extreme Ultraviolet Variability Experiment (EVE; Woods et al. 2012) instrument on the Solar Dynamics Observatory (SDO). We used level 3, version 5, daily averages data files of the solar irradiance at 58.4 nm available at the LISIRD website. The implication of using daily averages is that observations taken within the same day have the same converting factor (the g-factor) from brightness to column densities. As shown in Figs 5 and 6 (green line), variations of g-factor are smaller than those of the integrated *ARTEMIS* flux. For more specific details about the column density retrieval (such as formulas for the g-factor and solar irradiance), see Grava et al. (2018).

3 THE HELIUM EXOSPHERIC MODEL

To interpret the data, we used a modified version of the exospheric helium model described in Hurley et al. (2016). The model assumes that the helium atoms are injected into the dayside exosphere with a Maxwell–Boltzmann Flux distribution (Brinkmann 1970) with the nominal source rate of 8 × 10^6 cm^{-2} s^{-1} (scaled as the square cosine of solar zenith angle), or 4 per cent of the solar wind flux (the fraction of alpha particles in the solar wind), and uses a more rigorous method than previous publications to compute the surface temperature, validated by *LRO*'s Diviner measurements. The surface temperature model, described in Hurley et al. (2015), uses an analytic function that depends on the solar zenith angle, which in turn depends

on the Selenocentric Solar Ecliptic (SSE) latitude and longitude, extensively used in *Lunar Prospector* and *LADEE* data analysis. The SSE reference system is one centred on the Moon and where the *x*-axis points towards the Sun, the *z*-axis towards the ecliptic north, and the *y*-axis completes the orthogonal set. Therefore, longitudes in SSE coordinates correspond to LTs shifted by 180 degrees, i.e. a LT of 195° (or 13:00 LT) corresponds to an SSE longitude of 15°. SSE longitudes are sometimes referred to as subsolar longitudes. We will refer to LTs for the remainder of this paper. Compared to previous models, our surface temperature model better reproduces the effect of topography, especially important at the terminators. Our model uses a grid of 360x180x20 bins in, respectively, subsolar longitude, colatitude, and altitude (with altitude bins of 10 km). We have used two different accommodation coefficients α (equation 1), 1.0 and 0.75, to test whether or not the lunar helium is fully accommodated to the lunar surface. We also introduced a third model, called 'mixed', where we set $\alpha = 1.0$ on the dayside and $\alpha = 0.75$ on the nightside, to test the hypothesis that the accommodation coefficient may vary between day and night, with lower value of α at night (Leblanc & Chaufray 2011).

Fig. 3 shows the altitude profiles of the models considered for this study, for two LTs: 22:00 (squares) and 13:00 (circles). It is interesting to note how the 'mixed' model ($\alpha = 1.0$ on the dayside and $\alpha = 0.75$ on the nightside; red points) gives, on the dayside, such similar densities to the full thermal accommodation model (black points): the effect that α has in the structure of the exosphere is clearly dominated by the dayside. Fig. 3 shows another interesting effect of α, on the overall exospheric density. For the same source rate, the model with $\alpha = 0.75$ gives a denser exosphere (by a factor of ∼2) at the surface than the other two models. This is related to the effect of thermal accommodation on the velocity distribution of exospheric particles (Section 1.3), and can be understood in terms of interaction with the surface: the lower α is relative to 1.0, the more pre-impact energy is preserved by particles when hopping on the surface, and the lower the effect of the surface temperature on the post-impact energy (equation 1). In this way, α affects escape rates and spatial distribution. To better show this effect, we scaled all models to the number densities recorded by LACE during the nine lunations of its operations (Fig. 4). All three scaled models reproduce the LACE observations quite well, but the scaling factors (reported in the legend) are substantially different.

3.1 Pointing geometry

In order to compare the LAMP measurements with the model, we need to reconstruct the geometry of the observations, to derive, from the model, the predicted column density of the illuminated line of sight of each 2-min bin of data. We do that using the NAIF SPICE

Orbit 21032, LAMP_ENG_0413901707_02.fit (pitch_63), 2014-02-12T13:13:03.00 (119 s)
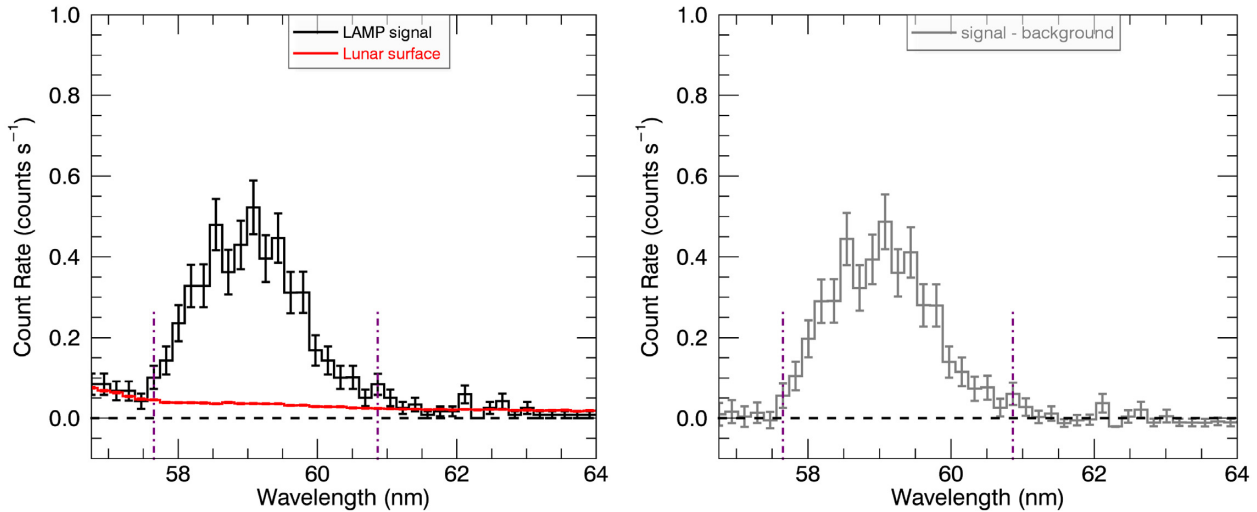

Figure 2. Left: spectrum of one lunar helium observation obtained with the spacecraft in sunlight looking at the lunar night side (black) and the background spectrum of the lunar night side obtained with the spacecraft in shadow (grey). Right: their difference. The dashed vertical lines encompass the region used to integrate the emission line. Error bars represent 1σ errors.
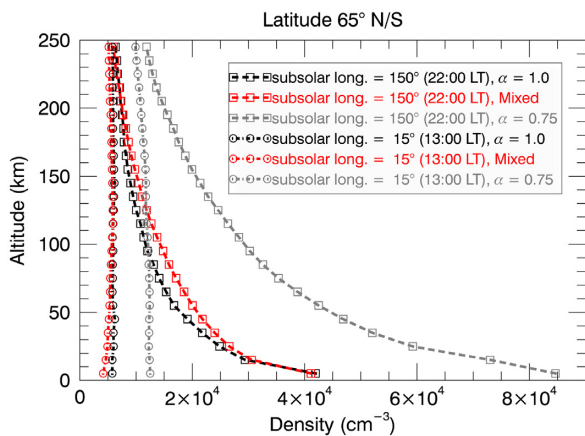

Figure 3. Comparison of model altitude profiles at $150°$ (squares) and $15°$ (circles) from the subsolar point (i.e. 22:00 and 13:00 LT, respectively) at $65°$ latitude North or South (the models are symmetric with respect to the equator). The term 'Mixed' refers to the model in which $\alpha = 1.0$ on the dayside and $\alpha = 0.75$ on the nightside.
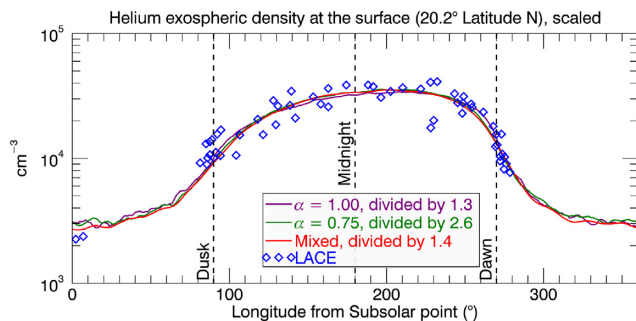
Figure 4. Diurnal profiles of exospheric helium density for our exospheric models scaled to match the diurnal profile recorded by LACE at the surface during nine lunations. Blue diamonds are digitized from fig. 2 of Hoffman et al. (1973). The legend reports the value by which we had to divide each model to match LACE. The term 'Mixed' refers to the model in which $\alpha = 1.0$ on the dayside and $\alpha = 0.75$ on the nightside.

toolkit (Acton 1996). As illustrated in Fig. 1, the line of sight of LAMP can sometimes traverse very different LTs. By integrating the helium density along the illuminated line of sight in this way (using SPICE-derived pointing coordinates), we can account for the different densities along a given line of sight.

For each 2-min bin, we have computed the position of the spacecraft and the pointing of the instrument in the above-mentioned SSE reference system. In it, longitudes are angles from the subsolar point and correspond to LT, where 1 h in LT corresponds to $15°$ in SSE longitude. SSE latitudes are computed from the subsolar point, but since this has a selenographic latitude of $1.5°$ North or South at most, they are practically equivalent to selenographic latitudes, and we refer to them from now on simply with 'latitudes'. We also computed the *LRO* position and LAMP pointing in Moon Mean Earth reference system, to obtain the selenographic longitudes of the points along the illuminated line of sight. The longitude is needed to search for any regions of enhanced outgassing (see Section 4.2). About 1 per cent of all the 2-min time bins have a negative brightness (and hence column density). These originate from the helium brightness being too dim and therefore from an oversubtraction of the background in a manner consistent with statistical probabilities. Since they represent a minor fraction of the data set, we discarded them.

3.2 Data–model comparison

Once the geometry of the observation is known, we integrate the model density along the line of sight and derive the predicted column density. We subdivided the space around the Moon in 24 1-h LT bins (where 6:00 means dawn and 18:00 means dusk), 24 15-degree selenographic longitude bins, and 18 10-degree latitude bins.

Since all of the four models are referred to the same, nominal, solar wind alpha particle source rate (8×10^6 cm^{-2} s^{-1}), each column density from the model needs to be scaled to match the real solar wind alpha particles flux (the main source for the lunar helium atoms). We used data from the twin spacecraft *ARTEMIS* (Acceleration, Reconnection, Turbulence, and Electrodynamics of Moon's Interaction with the Sun; Angelopoulos 2011), which orbit the Moon in a highly elliptical trajectory and measure charged
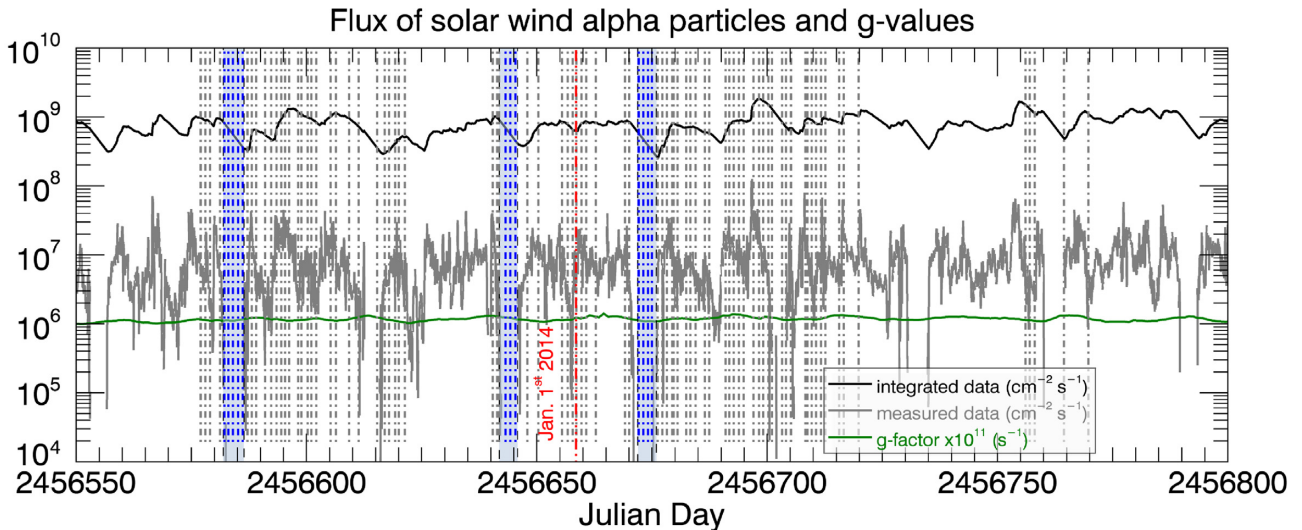
Figure 5. Grey line: actual solar wind alpha flux measured by *ARTEMIS*. Black line: a running integral of the actual data over 5 d. Green line: g-factors (multiplied by 10^{11}) derived from SDO/EVE. Light blue regions highlight times when *ARTEMIS* was inside the magnetospheric tail lobe and LAMP collected more than three orbits' worth of data. Vertical dashed lines are times of LAMP observations, colour-coded by whether (blue) or not (grey) *ARTEMIS* was inside the magnetospheric tail lobe and LAMP collected useful data. Vertical red line indicates 2014 January 1, for reference. Shown here is the first period of interest (2013 September 14–2014 May 22).
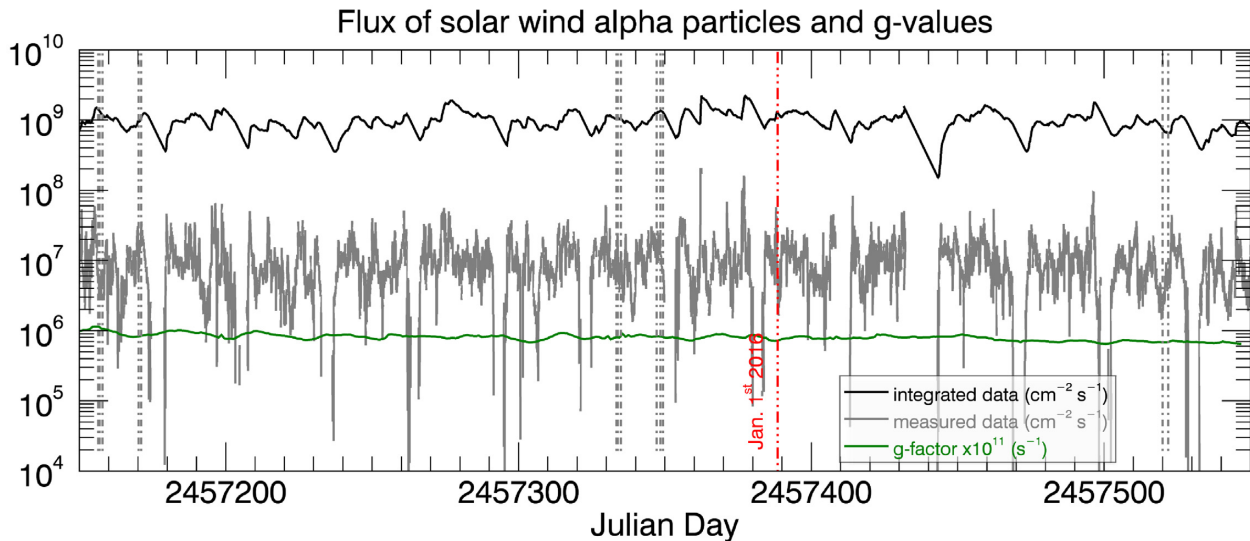
Figure 6. Same as Fig. 5 but for the second period of interest (2015 May 7–2016 June 10). Vertical red line indicates 2016 January 1, for reference. There are no LAMP measurements during magnetotail passages, hence these are not highlighted in blue like in Fig. 5.

particles from the solar wind and from the lunar tenuous ionosphere (e.g. Halekas et al. 2013). Figs 5 and 6 show the solar wind alpha particles flux measured with *ARTEMIS*' Electrostatic Analyzer (ESA) and its running integral. The latter is a factor of 102.37 greater than the measured flux since the running integral is performed over 5 d. The factor 102.37 is the effective multiplicative factor from the 5-d decay integration. It is equal to $5 \times 24 \times 3600/\mathrm{d}t$ where $\mathrm{d}t$ is the median Artemis time step in seconds. For each 2-min line of sight, we divide each modelled column density by the source rate of the model (8.0×10^6 cm^{-2} s^{-1}) and multiply it by the integrated solar wind alpha flux (divided by 102.37) for the corresponding day. We used the integrated flux instead of the instantaneous one for two reasons: (a) to account for the fact that lunar helium has been accumulating in the exosphere for days (the typical residence time is 4.5 d); (b)

to smooth out noisy fluctuations in the instantaneous data. Orbits within the same day have therefore the same scaling factor (besides having the same g-factor).

4 RESULTS

4.1 Thermal accommodation

Fig. 7 compares LAMP's observed column densities with those predicted by the three versions of our model. We calculated the Pearson correlation coefficient and the slope of a linear fit. The results are reported in Table 2. The Pearson correlation coefficient for all models is around 0.85. However, the slope of a linear fit reveals that the model with $\alpha = 1.0$ is the one that best reproduces a
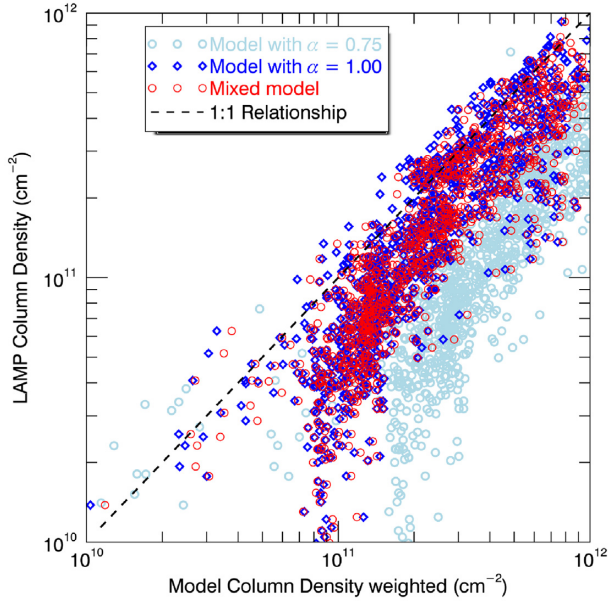
Figure 7. Scatter plot of LAMP column densities versus predicted column densities, from our three different models. The term 'Mixed' refers to the model in which $\alpha = 1.0$ on the dayside and $\alpha = 0.75$ on the nightside. There are about two dozens points for which LAMP signal was so low that the resulting column density is much lower than the predicted one. As mentioned in the text, these points are excluded from further analysis.

Figure 8. Histogram of the fraction of illuminated line of sight (l.o.s.) with respect to the total l.o.s. for all LAMP observations. This figure shows that, even though LAMP is pointing at the lunar nighttime surface, the majority of its line of sight is above illuminated (dayside) regions, where the difference between the $\alpha = 1.0$ model and the 'mixed' model is minimal.

Table 2. Lunar exospheric helium models used and their comparison with LAMP data. α is the accommodation coefficient, ρ is Pearson's correlation coefficient, and s is the linear fit slope. The error on all the slopes is 0.01.

α	ρ	s
0.75	0.86	0.30
0.75 at nightside; 1.0 in dayside	0.86	0.61
1.0	0.85	0.66

1:1 relationship between data and model (i.e. slope closest to 1.00). Therefore, we can state that the lunar helium exosphere is in full thermal accommodation with the lunar surface, and for the remainder of this paper we will compare LAMP column densities with the model with $\alpha = 1.0$. We note here that the reason the mixed model gives a slightly lower linear fit slope than the model with $\alpha = 1.0$ can be explained by the fact that a great fraction of the total lines of sight from the spacecraft to the Moon is illuminated – see Fig. 8. Fig. 9 shows the helium surface density resulting from this model. Note the peak in exospheric density at 2:00 am LT and high latitudes. This latitudinal trend is a consequence of several factors: the transport from day to night, the thermal accommodation, and the hop length.

4.2 Search for regions of enhanced outgassing

With the best model in hand, we can now press on and compare its column densities with those measured by LAMP, to uncover potential dependencies on selenographic coordinates and solar wind alpha flux. Since what LAMP measures is column density, interpretation of its data is achieved by looking at the ratio between measured column density and predicted column density. Figs 10, 11, and 12 show these
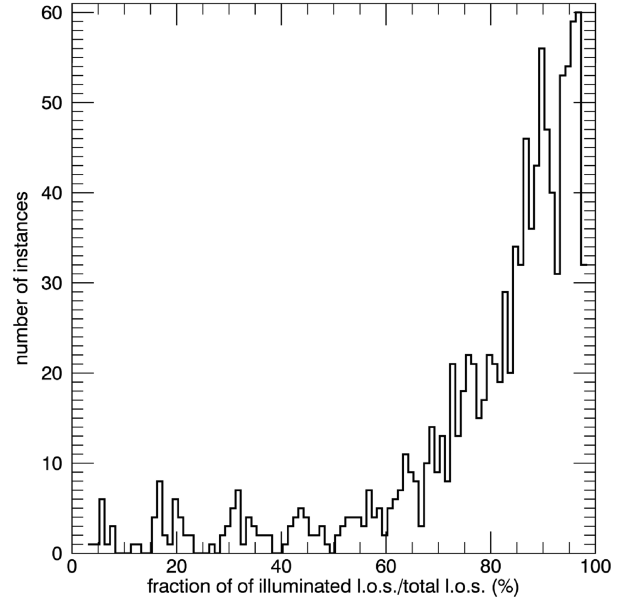
ratios versus three parameters: latitude, LT, and longitude of the shadow point, respectively. Points in each of these three figures are averages of the LAMP/model ratio over one of these three parameters regardless of the other two. For example, Fig. 10 shows averages of the LAMP/model ratio over latitudes regardless of longitudes and LTs, meaning that we averaged all ratios above that latitude bin regardless of their longitude and LT. The vertical error bars are standard deviations, while horizontal bars denote the length of the chosen latitude bin. We did not include lines of sight with less than two values in a given bin. Most of the points align themselves, within error bars, to the same constant value, which means that the exospheric model correctly reproduces the expected trends of helium density. There are some outliers at the Northern hemisphere, where the LAMP/model ratio is higher than 1.0 (Fig. 10). We shall return to this point at the end of Section 5.

Like in previous analysis of nadir-looking LAMP spectra (Feldman et al. 2012), we find no obvious dependence with latitude, nor it is expected given the dependence of helium exospheric density on the solar zenith angle.

Next, we show these same ratios in a 2D plot (Figs 13, 14, 15, and 16). Figs 13 and 14 show the LAMP/model average ratios and their standard deviations, respectively, as a function of LT, regardless of longitude. Figs 15 and 16, instead, show LAMP/model ratios and their standard deviations, respectively, over selenographic longitudes, regardless of LT. The predominance of data in the northern high latitudes is explained by *LRO*'s orbit, whose apoapsis is above the Moon's North Pole. Therefore, there are far more points with good SNR in the Northern hemisphere than in the southern one, given the longer time span spent near apoapsis versus periapsis and the larger spacecraft altitude at apoapsis offering longer columns to observe through. All the mid- and low-latitude observations were obtained with pitches and rolls of moderate angles, and the fact that they are all concentrated in the Western maria is a coincidence
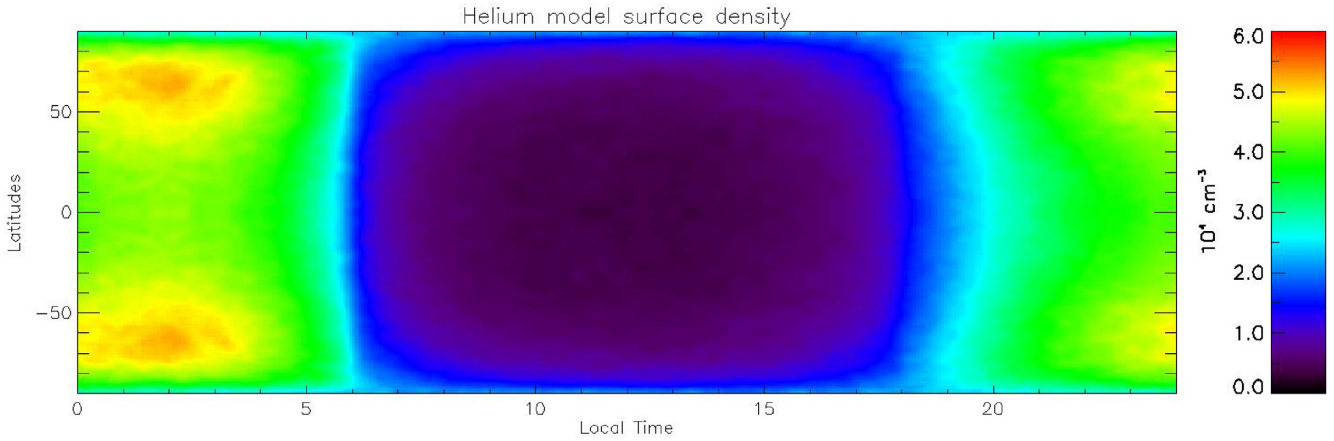
Helium model surface density

Figure 9. Surface density of helium from the model with $\alpha = 1.0$, with nominal source rate of 8×10^6 cm^{-2} s^{-1} at the subsolar point.
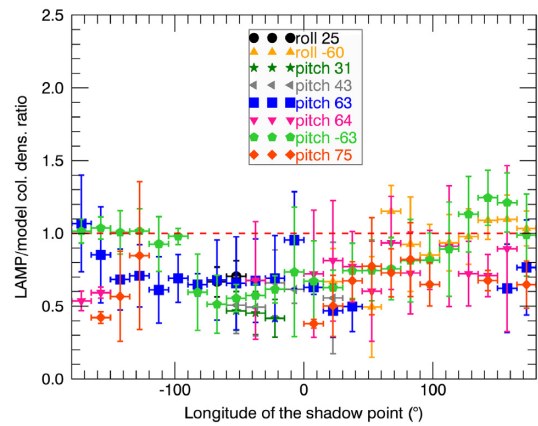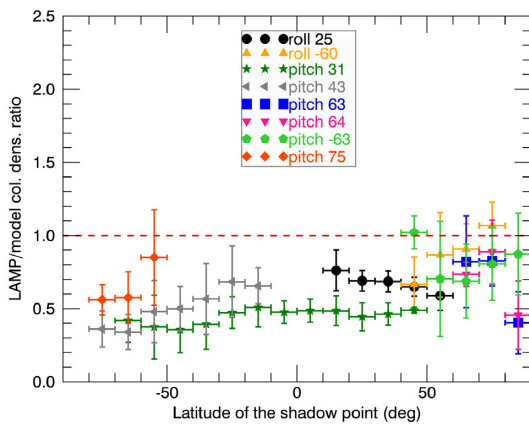

Figure 10. Ratio of column densities (measured/predicted) for all LAMP observations versus shadow point's latitude.

Figure 12. Same as Fig. 10 but with ratios plotted against shadow point selenographic longitude (negative longitudes correspond to the Western hemisphere).
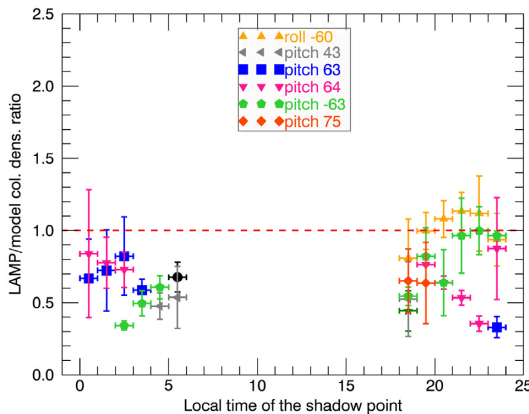

Figure 11. Same as Fig. 10 but with ratios plotted against shadow point LT. The number of points is considerably lower than that in previous figure because of the average over all latitudes and LTs.

(given *LRO*'s inertial orbital plane, the times spent in the terminator plane occur near a common lunar longitude during the years of data collection, drifting slowly year by year with orbit precession). Incidentally, this region, the Procellarum KREEP Terrane, contains one of the highest concentrations of ^{232}Th (up to 9 ppm; Jolliff et al. 2000), a parent of ^{4}He, and *LADEE*'s NMS measurements

have shown enhanced number densities of ^{40}Ar above that region (Benna et al. 2015). Two independent Monte Carlo simulations gave contradictory results regarding the origin of this 'bulge', with Hodges & Mahaffy (2016) explaining it with a lower activation energy of argon-40 with the lunar surface in that region, and Kegerreis et al. (2017) supporting the hypothesis that the 'bulge' is caused by a higher degassing rate of ^{40}Ar from that region. Given that both ^{40}Ar and ^{4}He are products of radioactive decay, and both diffuse from the interior through cracks and fissures in the upper crust, it is tempting to postulate that this region could have an enhanced degassing rate of helium too, compared to other regions. Moreover, circular fault systems around impact basins (with which the Procellarum area is replete) seem to be the best places for deep moonquakes to occur (Runcorn 1974), and these are related to degassing of radioactive elements. Interestingly, the detection of short-lived radon and polonium by the alpha particles spectrometers onboard the Apollo 15 and 16 command modules (Bjorkholm, Golub & Gorenstein 1973; Gorenstein, Golub & Bjorkholm 1974) also peaked above the edge of several maria (see fig. 2 in Gorenstein & Bjorkholm 1973), including the Oceanus Procellarum. LAMP data, however, show no signs of an exospheric enhancement in helium-4 number densities, even binning several observations by selenographic longitude (Figs 12 and 15). We will return to this important point in Section 5.
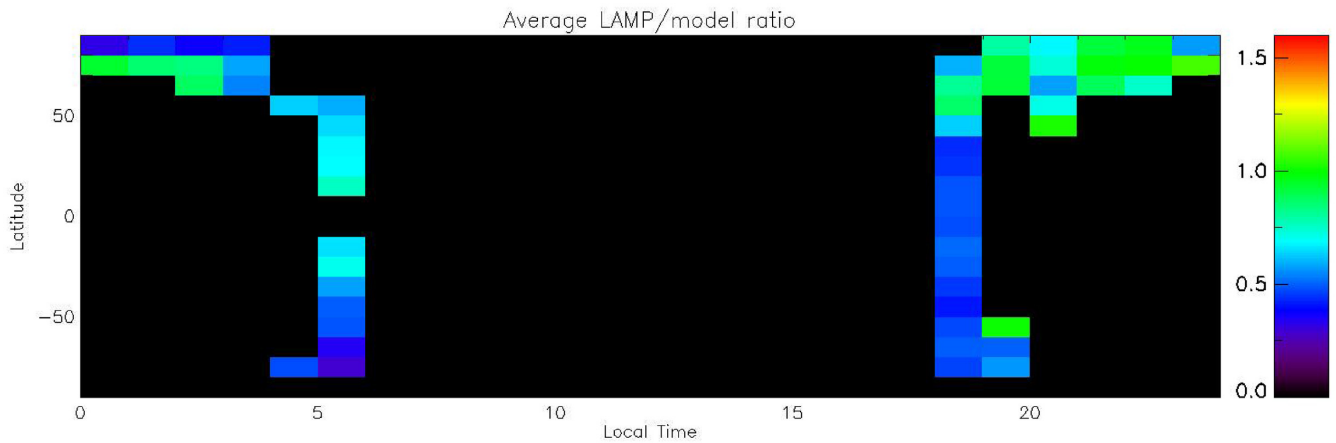
Figure 13. Average of the ratios LAMP/model regardless of longitude. The majority of our observations are restricted to nightside and terminators because, even if the spacecraft is in sunlight, LAMP always observes the lunar nightside.
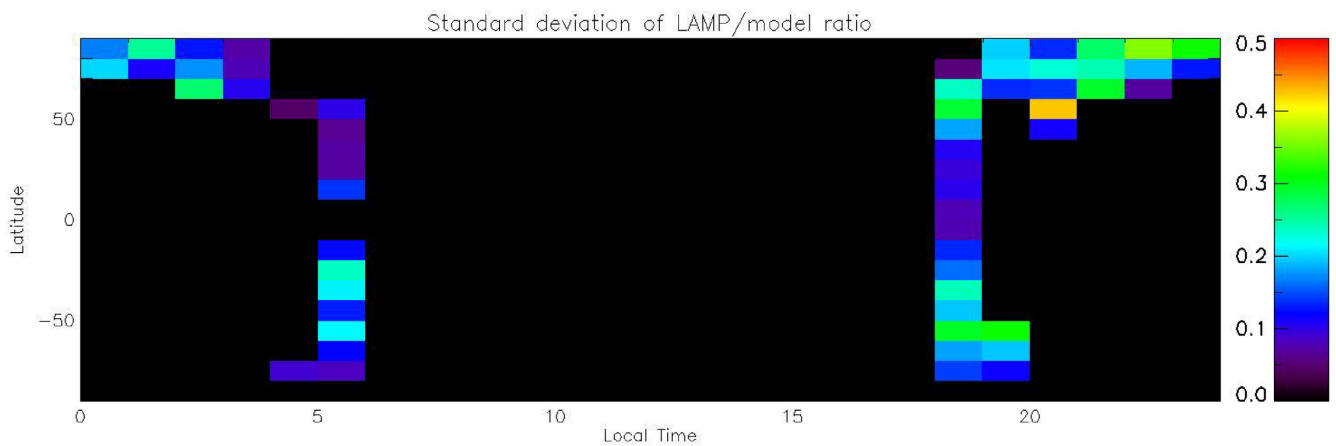

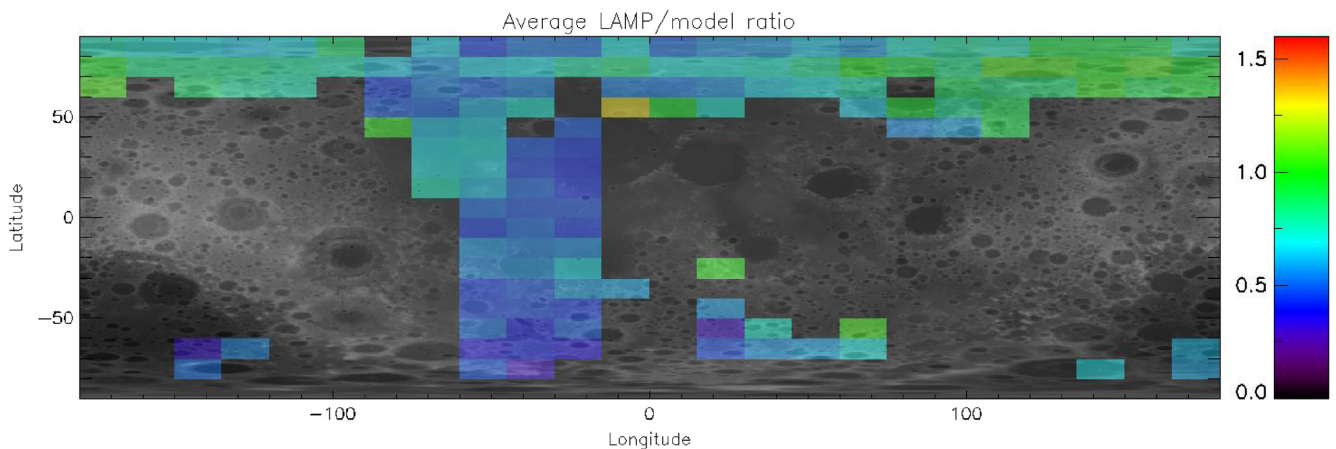**Figure 14.** Standard deviation of the ratios LAMP/model regardless of longitude.

Figure 15. Average of the ratios LAMP/model regardless of LTs. The background is a topography map from *LRO*'s LOLA (Lunar Orbiter Laser Altimeter). Only bins where LAMP collected signal are coloured.

4.3 Endogenic lunar helium degassing rate

The third aim of this campaign was to narrow down the uncertainty pertaining to the degassing rate of endogenic lunar helium. To do that, we have taken the averages of all the LAMP/model ratios for

a given orbit, and compared these averages to the solar wind alpha particles flux measured *in situ* by *ARTEMIS* (the integrated value – the black line in Figs 5 and 6). For this type of comparison, it is necessary to use the unscaled model: we take LAMP column density
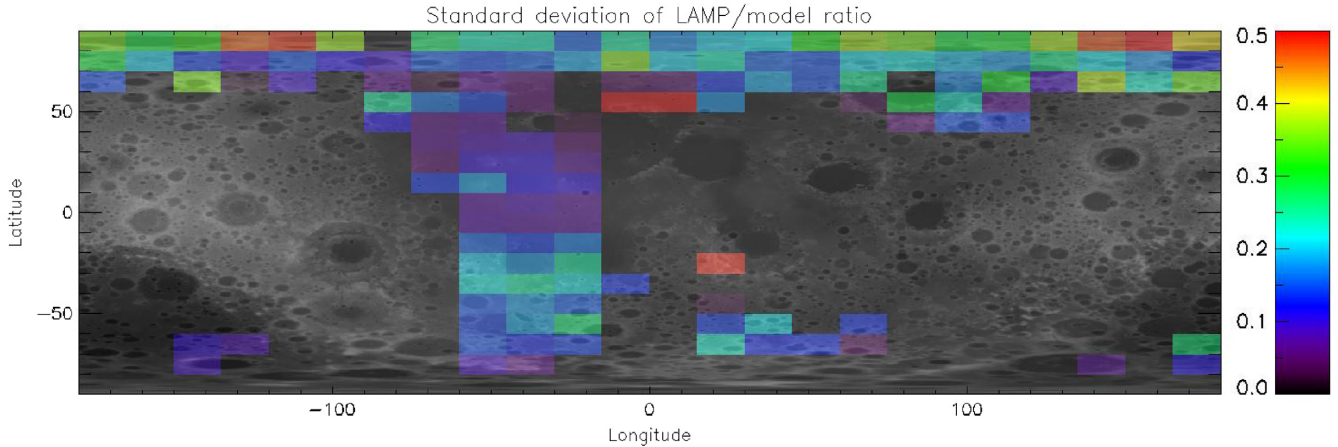
Figure 16. Standard deviation of the ratios LAMP/model regardless of LTs. The background is a topography map from *LRO*'s LOLA.
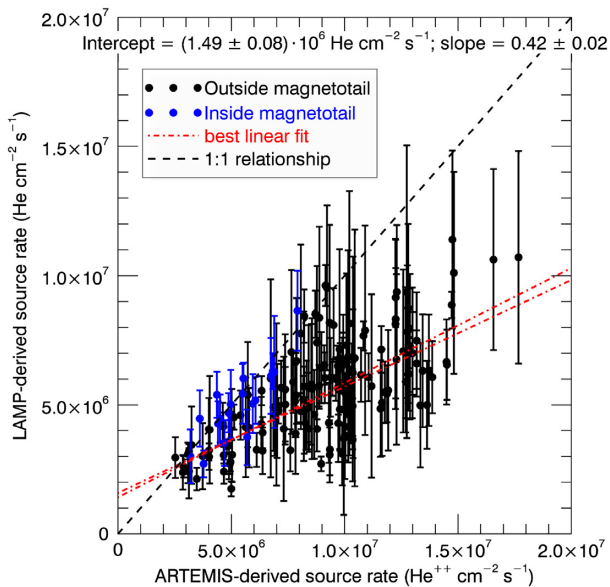

Figure 17. Scatter plot of source rates. Each point is the average of the LAMP/model ratios for a given orbit, and error bars are standard deviations. Blue points indicate data taken inside Earth's magnetotail. Red lines represent the linear fit (with errors) of the black points.

and we divide it by the column density of the model not scaled by the ARTEMIS integrated flux, and then multiply this ratio by the nominal source rate used in the model (8.0×10^6 cm^{-2} s^{-1}). In this way, we can derive the source rate compatible with the LAMP observations.

Fig. 17 shows the scatter plot of LAMP-derived source rate versus solar wind alpha particles flux. To quantify the relationship between the source rate derived from LAMP observations and the measured solar wind alpha particles flux, we performed a linear fit to the black points of Fig. 17. In doing so, we decided not to include in the fit the blue points of that figure, i.e. data taken while the Moon (and *LRO* and *ARTEMIS*) was inside Earth's magnetotail (blue regions and vertical lines in Figs 5 and 6). When this happens (about 5 d every month), *ARTEMIS* has no ability to collect data from the solar wind. Hence the abscissa, which is a running integral of *ARTEMIS*

data, is not well defined. We used IDL's *linfit.pro*, which performs the fit by minimizing the chi-square error statistic. The slope and the intercept of the linear fit represent two physical parameters of particular interest.

The intercept is the lunar endogenic source rate, i.e. the source which is still present even if the solar wind is deflected by Earth's magnetosphere. We interpret this to be the amount of helium degassing from the lunar subsurface: $(1.49 \pm 0.08) \times 10^6$ cm^{-2} s^{-1}, or $\sim$19 per cent of the solar wind alpha particles flux. This value is reduced compared to our previous analyses of LAMP data (Grava et al. 2016; Hurley et al. 2016), and is in agreement with analysis of *in situ* measurements of *LADEE*'s NMS (Benna et al. 2015), which quote a range of $(1.5 - 2.0) \times 10^6$ cm^{-2} s^{-1}, but is now better constrained.

The slope s of the linear fit represents the fraction of solar wind alpha particles that we detect as helium. The value $(1 - s)$, conversely, represents the fraction of helium atoms that LAMP cannot detect. We find that 58 per cent of the solar wind alpha particles flux is not detected by LAMP. We discuss the implication of these findings in Section 5.

4.4 Comparison with LACE

We can compare LAMP-constrained helium surface densities from our model with those measured *in situ* by LACE. To do so, we select all LAMP observations whose shadow point's latitude is within 18 and 22° N, for comparison with helium exospheric surface densities measured at LACE's location at 20° N. These happen to be grouped either at dawn or at dusk. Therefore, we averaged the LAMP-constrained helium exospheric density at the surface from our model (meaning that the exospheric density from the nominal, unscaled, model has been multiplied by the ratio between LAMP's and the model's line-of-sight column density). These two points are shown in Fig. 18 as black squares, together with LACE helium exospheric densities (blue diamonds) and previous LAMP measurements (horizontal green bar), from Stern et al. (2012). The LAMP-constrained exospheric densities at the surface from our model agree is within LACE values and slightly higher than previous LAMP observations, whose column densities were converted into exospheric surface densities using the Chamberlain's approach (Chamberlain 1963). The dawn/dusk ratio of the LAMP-retrieved surface densities is slightly lower ($\sim$1.8) than that from
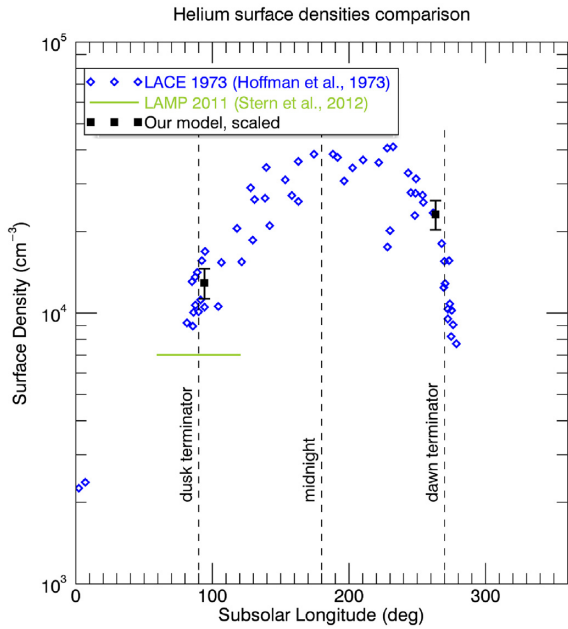
Helium surface densities comparison

Figure 18. Comparison between helium densities in the lunar exosphere at the surface. Blue points are *in situ* measurements by LACE (same as in Fig. 4); green horizontal bar indicates the LAMP-derived surface densities by Stern et al. (2012); black points with error bars are LAMP-constrained exospheric surface densities from our model for observations during which LAMP line of sight was pointed at latitudes 18–22° N. Black points at dawn correspond to averages over days 13, 14, and 15 of 2013 December, while black points at dusk correspond to averages over days 13, 14, and 15 of 2015 May.

LACE measurements (∼2.5). This ratio was predicted by Hodges & Johnson (1968) and explained with the non-adsorbing nature of helium (density *n* related to surface temperature *T* by the formula $n \sim T^{-5/2}$). These slight discrepancies may be ascribed to different solar wind conditions, different calibration methods, and different instruments (LAMP is a remote sensing instrument while LACE was an *in situ* instrument).

4.5 Exospheric density decay inside the magnetotail and recovery after egress

Fig. 19 shows the LAMP-constrained exospheric surface density as a function of time for those geomagnetic tail (magnetotail) crossings (light blue regions) for which more than three orbits' worth of LAMP data are available inside the magnetotail itself (see also Fig. 5). The grey line is the *ARTEMIS* integrated flux of solar wind alpha particles scaled to the density value at day 0, while the dashed black line is a 4.5-d exponential decay profile starting at day 0. Hollow squares are the individual 2-min bins, while filled squares and their error bars are their average and standard deviations, respectively. In general, two patterns can be distinguished in these panels:

(i) The exospheric surface density begins decreasing as soon as the Moon enters the Earth's magnetotail and the solar wind is effectively 'shut off'. This is consistent with the solar wind being the dominant source of lunar exospheric helium.

(ii) The exospheric surface density ramps up quickly soon after egress from the magnetotail (as soon as the solar wind alpha particles have access to the Moon). The exospheric recovery follows the trend of *ARTEMIS* integrated data quite well, with the exception perhaps

of panel b, where we note the average solar wind alpha particles flux was higher by a factor of ∼3 than other two magnetotail crossings.

All these points confirm earlier findings from Apollo measurements (Hodges & Hoffman 1974) that the exponential decay constant for the lunar helium exosphere is 4.5 d.

5 DISCUSSION

It is interesting to compare the endogenic source rate of helium consistent with these LAMP observations, $(1.49 \pm 0.08) \times 10^6$ cm^{-2} s^{-1}, with theoretical estimates based on the known abundance of thorium and uranium within the Moon. From the amount of radionuclides of interest expected to be present in the lunar interior (230 ppb for ^{232}Th and 60 ppb for ^{238}U, according to Taylor & Jakes 1974), Hodges (1977b) estimated a total helium production (in the interior of the Moon) of 177 ton yr^{-1}. Assuming the same degassing fraction for ^{40}Ar (6 per cent), Hodges predicted a degassing rate of 11 ton yr^{-1}. Our source rate, corresponding to (119 ± 6) ton yr^{-1} assuming degassing from the whole lunar surface, is roughly a factor of 10 greater than Hodges' estimate (∼67 per cent of the total helium production rate in the lunar interior). Part of the discrepancy is likely ascribed to the fact that degassing of native helium is, like ^{40}Ar, sporadic. Another explanation could be that helium is degassing from the lunar interior at a higher rate than argon-40. This is perhaps not surprising, given that helium is 10 times lighter than argon, and is consistent with what is observed on Earth, where the degassing rate for ^{4}He is twice that of ^{40}Ar (Krasnopolsky, Chakrabarti & Gladstone 1993).

The absence of a detectable 'plume' of helium at the Procellarium KREEP Terrane in the Western maria (see Fig. 15) is consistent with *LADEE*'s NMS non-detection of a helium enhancement in this same region, despite NMS having detected an enhancement in ^{40}Ar there (Benna et al. 2015). Fig. 20 shows the temporal evolution of helium exospheric density for a set of simulations we performed where we released 1000 kg of helium at the subsolar point and at mid-night. This additional dumping corresponds to ∼50 h's worth of solar wind alpha particles, or ∼3 d's worth of our inferred endogenic release rate. After a couple of hours at most from the sudden release, the increased helium density (over the nominal exosphere) is independent of the release location. The rapid redistribution of helium plays a crucial role. These simulations show that, in order to be detected by LAMP, a plume of helium would have to be substantial, and the spacecraft would have to fly close to it within a couple of hours at most.

Finally, it is noteworthy to discuss the nature of the ∼58 per cent of solar wind alpha particles that LAMP could not detect. This fraction is higher than the ∼40 per cent reported by Hodges (1975) from analysis of LACE. There are several explanations for this 'missing helium', and they are not mutually exclusive. One explanation is that these are solar alpha particles that are backscattered, either as ions or neutrals, upon contact with the lunar surface, therefore bouncing off to space immediately. Several spacecraft (*Kaguya*, *Chandrayaan-1*, *IBEX*, and *ARTEMIS* itself) have measured the fraction of solar wind protons reflecting off the lunar surface (McComas et al. 2009; Futaana et al. 2010; Saito et al. 2010; Lue et al. 2018). The vast majority of protons that backscatter do so as Energetic Neutral Atoms (Allegrini et al. 2013), with only a minor fraction (< 1 per cent) backscattered as ions (Saito et al. 2008). As much as 20 per cent of the incoming solar wind protons can be backscattered as neutrals (Wieser et al. 2009), but the fraction for alpha particles is likely much lower, or ∼1 per cent (Vorburger et al. 2014). Another explanation is that the solar wind alpha particles are implanted in grains freshly
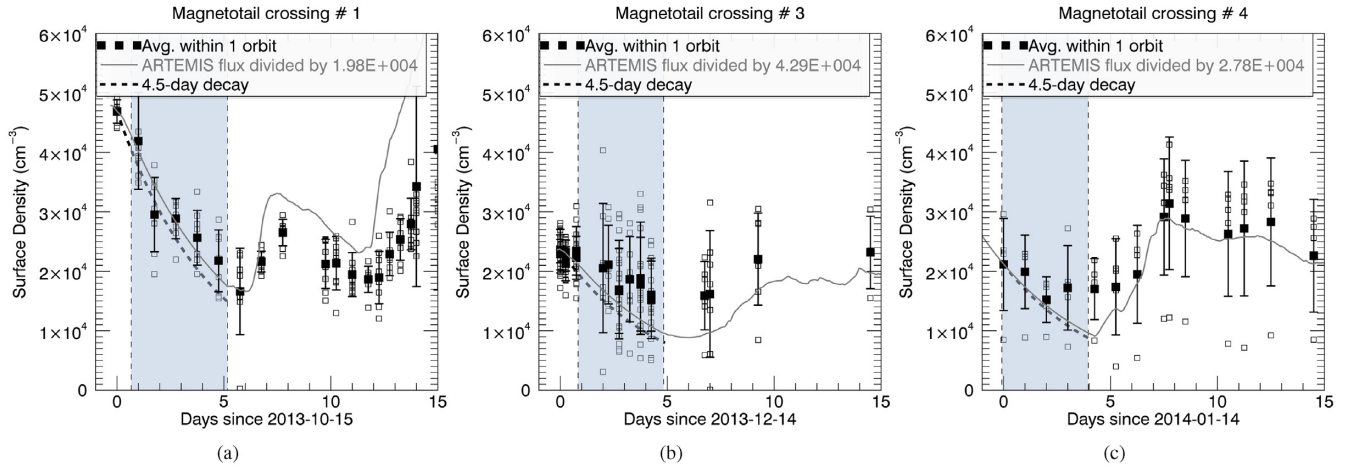
Figure 19. LAMP-constrained surface densities during three magnetotail crossings (light blue regions, corresponding to light blue regions in Fig. 5). Surface densities are derived from the nominal model multiplied by the LAMP/model ratio of column densities. Hollow squares represent individual 2-min bins LAMP observations. Filled squares and their error bars are their average and standard deviations, respectively. The grey line is *ARTEMIS* integrated flux of solar wind alpha particles, while the dashed black line inside the light blue region is a 4.5-d exponential decay profile. Both the grey line and the black dashed line have been scaled to the density at day 0 (the scaling factor for *ARTEMIS* is reported in the legends).
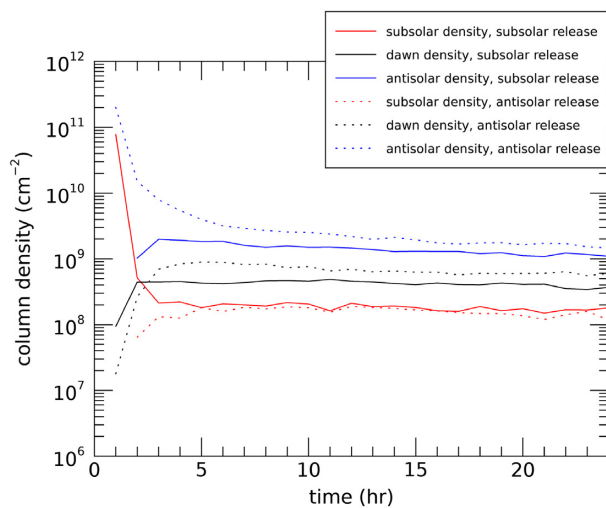

Figure 20. Temporal evolution of a helium exosphere with 100 times the nominal source rate of our models, or 8×10^8 cm^{-2} s^{-1}, ejected at the subsolar point (solid lines) or at the antisolar point (dashed lines). For each release, densities are shown at three different locations (terminator, subsolar, and antisolar).

exposed to the solar wind (and hence not saturated with helium) by the relentless reworking of the upper centimeters of the lunar regolith (e.g. Costello, Ghent & Lucey 2018). In this case, the release of a helium atom may not occur shortly after the implantation of the solar wind alpha particle. Incidentally, if it takes days for the neutral atom to be released, then this might explain part of the discrepancy between the *ARTEMIS* flux and LAMP-derived exospheric helium densities shown in panel (b) of Fig. 19. The last hypothesis is that the helium atoms are trapped in satellite orbits. As the models of Hodges (1977a, 1978) have shown, when considering the gravitational potential of the Earth and the Sun and the solar radiation pressure (Potter & Morgan 1987), perturbations to helium atoms' trajectories lead to the formation of a lunar corona that actually contains more atoms

than the near-surface exosphere. Helium atoms with velocity just 20 per cent of escape speed at the lunar surface have the potential to reach these satellite orbits, with periapsis much greater than the lunar radius. These atoms spend their lifetime in orbit around the Moon until they are eventually ionized (after months), and some end up in Earth's exosphere. The fraction of these particles with periapsis below *LRO*'s apoapsis (∼180 km) is arguably small, given that this corona may extend to tens of lunar radii (Hodges 1977a). Therefore, it is unlikely that this population contributes to the missing 58 per cent of solar wind. Still, this population could account for some of the discrepancies between LAMP and the model's column densities at northern latitudes (Fig. 10), which is where the *LRO* apoapsis is.

6 CONCLUSIONS

We presented lunar exospheric helium abundance results from a detailed atmospheric observing campaign performed by the LAMP instrument onboard of *LRO*. The *LRO* was tilted sideways and along the direction of motion to allow LAMP, the EUV/FUV imaging spectrograph, to detect the resonant scattering line of helium (He I at 58.4 nm) for several minutes each orbit. More than 170 orbits are analysed in this paper and the results are summarized here:

(i) Our simulations confirm that the lunar exospheric helium is well described by a Maxwell–Boltzmann flux speed distribution with full thermal accommodation over the entirety of the lunar surface.

(ii) Comparison with solar wind alpha particles flux measured *in situ* by the *ARTEMIS* twin spacecraft confirms that the main source of lunar exospheric helium is solar wind alpha particles, and derives a value for degassing of native lunar helium (as product of radioactive decay of ^{232}Th and ^{238}U within the lunar crust) which is (19 ± 1) per cent that of the solar wind alpha particles flux. The resulting endogenic source rate translates to $(1.49 \pm 0.08) \times 10^6$ cm^{-2} s^{-1}, consistent with the lower end of the range resulting from *LADEE*'s NMS measurements (Benna et al. 2015), but with reduced uncertainty. Integrated over the entire lunar surface and assuming a continuous degassing, our value corresponds to (119 ± 6) ton yr^{-1}. This value is about a factor of 10 higher than the estimate from

Hodges ([1977b](#)) based on Apollo 17 LACE *in situ* measurements of helium exospheric density, and the assumption that the pathway for degassing of helium is the same as that for ^{40}Ar, another radiogenic element. Our discrepancy may indicate that this assumption is not correct, and hence helium degasses at a higher rate than argon, or that degassing occurs sporadically, like for argon.

DATA AVAILABILITY

LAMP EDR files used in this work are publicly available through the NASA Planetary Data System archive at https://pds-imaging.jpl.nasa.gov/volumes/lro.html. Solar irradiances from SDO/EVE at 58.4 nm are available on the website of the LASP Interactive Solar Irradiance Data Center at http://lasp.colorado.edu/lisird/data/sdo_eve_ssi_1nm_l3/. Solar wind alpha particles flux from *ARTEMIS* ESA is available on the website of ARTEMIS at http://artemis.ssl.berkeley.edu/. Table in the Supplemental Material lists the LAMP EDR files used, along with the time frame (in UT) that contains the data of interest for this work; the type of *LRO* maneuver; the g-factor from SDO/EVE used to convert brightness into column density; and the integrated solar wind alpha particles flux from *ARTEMIS*/ESA.

REFERENCES

Acton C. H., 1996, Planet. Space Sci., 44, 65
Allegrini F. et al., 2013, Planet. Space Sci., 85, 232
Angelopoulos V., 2011, Space Sci. Rev., 165, 3
Banks P. M., Johnson H. E., Axford W. I., 1970, Comments Astrophys. Space Phys., 2, 214
Barth C. A., 1969, Appl. Opt., 8, 1295
Benna M., Mahaffy P. R., Halekas J. S., Elphic R. C., Delory G. T., 2015, Geophys. Res. Lett., 42, 3723
Benson J., Freeman J. W., Hills H. K., 1975, In: Lunar and Planetary Science Conference Proceedings, Vol. 3. Pergamon Press, Inc., New York, p. 3013
Bjorkholm P., Golub L., Gorenstein P., 1973, Science, 180, 957
Brinkmann R. T., 1970, Planet. Space Sci., 18, 449
Broadfoot A. L., Shemansky D. E., Kumar S., 1976, Geophys. Res. Lett., 3, 577
Buhler F., Eberhardt P., Geiss J., Meister J., Signer P., 1969, Science, 166, 1502
Chamberlain J. W., 1963, Planet. Space Sci., 11, 901
Chin G. et al., 2007, Space Sci. Rev., 129, 391
Cook J. C., Stern S., 2014, Icarus, 236, 48
Cook J. C., Stern S. A., Feldman P. D., Gladstone G. R., Retherford K. D., Tsang C. C. C., 2013, Icarus, 225, 681
Costello E. S., Ghent R. R., Lucey P. G., 2018, Icarus, 314, 327
Feldman P. D. et al., 2012, Icarus, 221, 854
Freeman J. W., Benson J. L., 1977, Phys. Earth Planet. Inter., 14, 276
Futaana Y. et al., 2010, J. Geophys. Res., 115, A10248
Gladstone G. R. et al., 2010, Space Sci. Rev., 150, 161
Gorenstein P., Bjorkholm P., 1973, Science, 179, 792
Gorenstein P., Golub L., Bjorkholm P., 1974, Science, 183, 411
Grava C. et al., 2016, Icarus, 273, 36

Grava C., Pryor W. R., Feldman P. D., Retherford K. D., Gladstone G. R., Greathouse T. K., 2018, A&A, 616, A159
Halekas J. S., Poppe A. R., Delory G. T., Sarantos M., McFadden J. P., 2013, J. Geophys. Res., 118, 81
Hartle R. E., Thomas G. E., 1974, J. Geophys. Res., 79, 1519
Hartle R. E., Curtis S. A., Thomas G. E., 1975, J. Geophys. Res., 80, 3689
Hodges R. R. J., 1972, Planet. Space Sci., 20, 1849
Hodges R. R. J., 1973, J. Geophys. Res., 78, 8055
Hodges R. R. J., 1975, Moon, 14, 139
Hodges R. R. J., 1977a, In: Lunar and Planetary Science Conference Proceedings, Vol. 1. Pergamon Press, Inc., New York, p. 537
Hodges R. R. J., 1977b, Phys. Earth Planet. Inter., 14, 282
Hodges R. R. J., 1978, In: Lunar and Planetary Science Conference Proceedings, Vol. 9. Pergamon Press, Inc., New York, p. 1749
Hodges R. R. J., 1980a, J. Geophys. Res., 85, 164
Hodges R. R., 1980b, J. Geophys. Res., 85, 223
Hodges R. R. J., Hoffman J. H., 1974, Geophys. Res. Lett., 1, 69
Hodges R. R. J., Johnson F. S., 1968, J. Geophys. Res. Planets, 73, 7307
Hodges R. R. J., Mahaffy P. R., 2016, Geophys. Res. Lett., 43, 22
Hodges R. R. J., Hoffman J. H., Yeh T. T. J., Chang G. K., 1972, J. Geophys. Res., 77, 4079
Hodges R. R. J., Hoffman J. H., Johnson F. S., Evans D. E., 1973, In: Lunar and Planetary Science Conference Proceedings, Vol. 4. Pergamon Press, Inc., New York, p. 2855
Hodges R. R. J., Hoffman J. H., Johnson F. S., 1974, Icarus, 21, 415
Hoffman J. H., Hodges R. R. J., Johnson F. S., Evans D. E., 1973, In: Lunar and Planetary Science Conference Proceedings, Vol. 4. Pergamon Press, Inc., New York, p. 2865
Hunten D. M., Roach F. E., Chamberlain J. W., 1956, J. Atmos. Terr. Phys., 8, 345
Hunten D. M., Morgan T. H., Shemansky D. E., 1988, The Mercury Atmosphere. University of Arizona Press, Tucson, AZ, p. 562
Hurley D. M. et al., 2016, Icarus, 273, 45
Hurley D. M., Sarantos M., Grava C., Williams J.-P., Retherford K. D., Siegler M., Greenhagen B., Paige D., 2015, Icarus, 255, 159
Jolliff B. L., Gillis J. J., Haskin L. A., Korotev R. L., Wieczorek M. A., 2000, J. Geophys. Res., 105, 4197
Kegerreis J. A., Eke V. R., Massey R. J., Beaumont S. K., Elphic R. C., Teodoro L. F., 2017, J. Geophys. Res., 122, 2163
Killen R. M., 2002, Meteorit. Planet. Sci., 37, 1223
Kockarts G., 1973, Space Sci. Rev., 14, 723
Krasnopolsky V. A., Chakrabarti S., Gladstone G. R., 1993, J. Geophys. Res., 98, 15061
Kumar S., 1976, Icarus, 28, 579
Leblanc F., Chaufray J. Y., 2011, Icarus, 216, 551
Lue C., Halekas J. S., Poppe A. R., McFadden J. P., 2018, J. Geophys. Res., 123, 5289
McComas D. J. et al., 2009, Geophys. Res. Lett., 36, L12104
Nakamura Y., Latham G. V., Dorman H. J., Ibrahim A. B. K., Koyama J., Horvath P., 1979, In: Lunar and Planetary Science Conference Proceedings, Vol. 3. Pergamon Press, Inc., New York, p. 2299
Potter A. E., Morgan T. H., 1987, Icarus, 71, 472
Runcorn S. K., 1974, In: Lunar and Planetary Science Conference Proceedings, Vol. 3. Pergamon Press, Inc., New York, p. 3115
Saito Y. et al., 2008, Geophys. Res. Lett., 35, L24205
Saito Y. et al., 2010, Space Sci. Rev., 154, 265
Shemansky D. E., 1980, J. Geophys. Res., 85, 221
Shemansky D. E., Broadfoot A. L., 1977, Rev. Geophys. Space Phys., 15, 491
Smith G. R., Shemansky D. E., Broadfoot A. L., Wallace L., 1978, J. Geophys. Res., 83, 3783
Stern S. A., Retherford K. D., Tsang C. C. C., Feldman P. D., Pryor W., Gladstone G. R., 2012, Geophys. Res. Lett., 39, L12202
Taylor S. R., Jakes P., 1974, In: Lunar and Planetary Science Conference Proceedings, Vol. 2. Pergamon Press, Inc., New York, p. 1287
Vorburger A., Wurz P., Barabash S., Wieser M., Futaana Y., Holmström M., Bhardwaj A., Asamura K., 2014, J. Geophys. Res., 119, 709
Wieser M. et al., 2009, Planet. Space Sci., 57, 2132

Wilcox J. M., Schatten K. H., Ness N. F., 1967, J. Geophys. Res., 72, 19
Woods T. N. et al., 2012, Sol. Phys., 275, 115

SUPPORTING INFORMATION

Supplementary data are available at *MNRAS* online.

Tab_full.dat.

Please note: Oxford University Press is not responsible for the content or functionality of any supporting materials supplied by the authors.

Any queries (other than missing material) should be directed to the corresponding author for the article.

This paper has been typeset from a TeX/LaTeX file prepared by the author.